COunterfactual Reasoning for Temporal EXplanations: Plausible and Robust Explanations for EEG-Based Seizure Detection

Anonymous authors
Paper under double-blind review

Abstract

Identifying the drivers of change in time-sensitive domains like healthcare is critical for reliable decision-making, yet explanations must account for both temporal dynamics and structural complexity. While counterfactual explanations are well-studied for static data, existing methods often fail in dynamic, spatio-temporal settings, producing implausible or temporally inconsistent explanations. To address this, we introduce COunterfactual Reasoning for Temporal EXplanations (CORTEX), a search-based explainer for multivariate time series modeled as spatio-temporal graphs, tailored to seizure detection from EEG recordings. CORTEX generates temporally robust and plausible counterfactuals by retrieving relevant past instances and sieving them via structural dissimilarity, temporal distance, and instability. Evaluated on clinical seizure detection data, CORTEX outperforms state-of-the-art methods with a 2.73× improvement in validity and 5.32× in fidelity, and achieves zero implausibility, demonstrating consistency and practical relevance. By shifting the focus from mere validity to plausible and time-consistent explanations, CORTEX enables more reliable and controllable counterfactual explanations.

1 Introduction

Understanding the temporal evolution of a model's prediction is critical for trust and accountability, especially in sensitive domains like healthcare, where abrupt changes in a patient's physiological state – e.g, those measured by Electroencephalography (EEG) – require timely intervention. Counterfactual explanations (Wachter et al., 2017) are a promising approach to provide actionable recourse to the end-user.

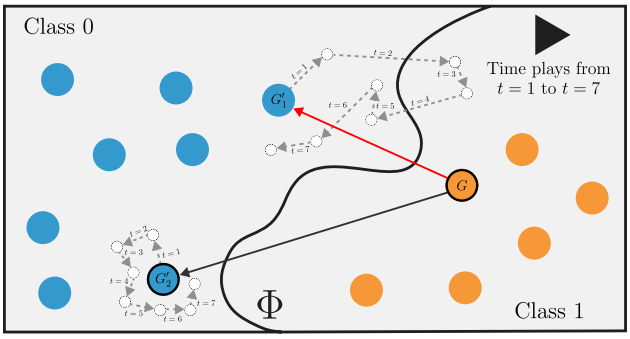

Figure 1: **Gist of CORTEX: When choosing counterfactuals in dynamic contexts, consider temporal evolution alongside similarity.** Given a graph G, G'_1 and G'_2 are two plausible counterfactual candidates. However, G'_1, as time goes by, has a "chaotic" trajectory; meanwhile, G'_2 has a more confined movement. We prefer G'_2 as counterfactual for G since it is likely to remain in the counterfactual class over time (i.e., to be more stable, temporally robust). To simplify the presentation, we have only depicted the change trajectories of G'_1 and G'_2 over time.

However, while common for static data, their application to multivariate time series is limited. Existing methods fall short by focusing on feature modifications without preserving underlying implicit correlations (Ates et al., 2021) or by restricting modifications to predefined deviation intervals (Yamaguchi et al., 2024). These approaches neither reflect the spatio-temporal structure nor focus on the structural differences that drive model outcome changes, making them fundamentally inadequate for dynamic, autoregressive contexts where modifications to past observations propagate and influence future trajectories.

To effectively illustrate the distinction between static and spatio-temporal counterfactual explanations in our scenario, we provide the following example (best viewed in color):

Static counterfactual:
"If the avg. slow-wave activity was 20% lower and the signal variability was 10% lower across the EEG measurement, then the patient wouldn't have had any epileptic seizure."

Spatio-temporal counterfactual:
"If, in the last 5 seconds of EEG activity, the avg. power of the low-frequency activity (slow-waves) in the right temporal lobe was 15% lower and the signal variability (variance) in the frontal lobe was 5% higher, then the patient wouldn't have had an epileptic seizure."

Legend: feature, time, space

This highlights the complexity of the spatio-temporal counterfactual: i.e., it must not only address three dimensions of explainability (feature, time, and space) but also explicitly process data inherently structured by these dimensions and account for temporal-dependencies from past to future.

In this paper, we address the challenge of producing robust temporal graph counterfactual explanations for multivariate time series, tailored to epileptic seizure detection from EEG data. We propose a novel search-based explainer, COunterfactual Reasoning for Temporal EXplanations (CORTEX). To account for the relationship among feature, time, and space, we represent the time series as spatio-temporal graphs and produce counterfactuals on them.

Since the underlying dynamics of EEG readings can be unknown, it might be unfeasible to produce plausible counterfactuals from scratch. Hence, CORTEX draws counterfactuals from previously observed robust states (see Figure 1), and then ranks them according to structural similarity, temporal distance, and temporal robustness.

This paper makes the following key contributions:

(1) A new paradigm for temporal counterfactuals. We introduce CORTEX, the first framework designed to generate counterfactual explanations that are not only valid but also plausible and temporally robust. Unlike prior methods that treat time series as static features or aggregate snapshots, CORTEX explicitly leverages the spatio-temporal nature of the data to ensure coherent, realistic explanations.

(2) Formalizing temporal robustness as a desideratum. We define and operationalize the concept of temporal robustness – the requirement that a counterfactual remains in the target class over time – via phase trajectory analysis of model predictions. This extends the standard desiderata of counterfactual explanations (Guidotti, 2022) to dynamic settings, providing a new principle for designing explainers in autoregressive domains.

(3) Demonstrated reliability in clinical time series. On EEG-based seizure detection, CORTEX consistently yields explanations that are both more faithful and more realistic than SoTA (5.32× improvement in fidelity, and zero implausibility). By grounding explanations in temporally robust, historically observed states, CORTEX enables actionable and reliable recourse in high-stakes applications such as healthcare.

2 Preliminaries

Let $\mathcal{G}$ describe the (finite) universe of graphs. Let $G = (X \in \mathbb{R}^{n \times d}, A \in \mathbb{R}^{n \times n}) \in \mathcal{G}$ be a graph with node feature matrix X and (weighted) adjacency matrix A, where n is the number of nodes, and d is the feature dimensionality. Let $\Phi : \mathcal{G} \to Y$ be a (already-trained) classification model, where Y is the set of target labels.

Note that the following assumes the reader understands that counterfactual explainability is a post-hoc method applied to Φ, i.e., after Φ has been trained.

Definition 1 (Static graph counterfactual) *Given Φ and $G \in \mathcal{G}$, a counterfactual for G is found as follows (Jiang et al., 2024; Prado-Romero et al., 2024b):*

$$\underset{\substack{G' \in \mathcal{G} \\ \Phi(G') \neq \Phi(G)}}{\arg\min} \; M(G, G') \,, \tag{1}$$

where $M : \mathcal{G} \times \mathcal{G} \to \mathbb{R}_{\geq 0}$ is an optimization metric, generally expressed in dissimilarity terms.

According to Guidotti (2022), counterfactuals should satisfy validity, minimality, proximity, plausibility, actionability, and causality. Note how Equation (1) satisfies the first three desiderata. While all these properties are important, the last three are seldom treated in other works. We argue that actionability and causality are more related to privacy literature – i.e., actionability ensures that changes only affect modifiable features, and causality requires to preserve any known causal feature relationships, usually formalized through structural causal models – and thus not treated in this paper. Contrarily, plausibility is the most overlooked desideratum because it enforces the counterfactuals be in-distribution of the real data, a phenomenon that learning-based, especially generative, explainers cannot always guarantee (see Ma et al. (2022); Prado-Romero et al. (2024a)).

Taken inspiration from Guidotti (2022) and the definition of counterfactual robustness (Jiang et al., 2024), we introduce an additional desideratum, namely *temporal robustness*, which is essential to ensure robustness of counterfactual explanations in dynamic settings. Temporal robustness requires that counterfactuals remain consistently classified by Φ over time, i.e., they do not lie in non-robust or transition regions of the feature space. In other words, temporal robustness is needed to guarantee that the generated counterfactual does not immediately revert to an anomalous state as the time series evolves. Without this property, the counterfactual would lose practical relevance, since its validity would not persist under the natural temporal dynamics of the system.

Before we extend the notion of counterfactuals for spatio-temporal graphs, let us define what a time (finite) graph is: i.e., a graph $G_{t_i} = (X_{t_i} \in \mathbb{R}^{n_{t_i} \times d_{t_i}}, A_{t_i} \in \mathbb{R}^{n_{t_i} \times n_{t_i}})$ where n_{t_i} is the number of nodes at time $t_i \in \mathbb{N}$. Now the graph universe $\mathcal{G}$ contains all possible time graphs.

Definition 2 (Temporally robust graph counterfactual) *Given $G_{t_i} \in \mathcal{G}$, Φ, and an optimization metric $M : \mathcal{G} \times \mathcal{G} \to \mathbb{R}_{\geq 0}$ (e.g., dissimilarity, temporal distance), a counterfactual for G_{t_i} satisfies validity, minimality, proximity, and temporal robustness if*

$$\underset{\substack{G_{t_j} \in \{\mathcal{G}\}_{<t_i} \\ \Phi(G_{t_j}) \neq \Phi(G_{t_i})}}{\arg\min} \quad M(G_{t_i}, G_{t_j}) \;\; s.t. \;\; S_\Phi(G_{t_j}) \leq \epsilon \,, \tag{2}$$

where $\{\mathcal{G}\}_{<t_i}$ denotes the set of graphs prior to time t_i,[1] $S_\Phi : \mathcal{G} \to [0, 1]$ is an instability score *of Φ on a graph (intended as a lack of temporal robustness), and ϵ is an upper bound on instability. Smaller values of S_Φ indicate more temporally robust predictions.*

In words, Definition 2 selects among past candidates that flip Φ's decision, choosing the closest one that also exhibits sufficiently low predictive volatility. Plausibility can be guaranteed by construction if we restrict the universe of time graphs $\mathcal{G}$ to the observed dataset $\mathcal{D}$, as is typical in search-based explainers (see Section 3).

[1]Note that it is meaningless to produce counterfactuals that succeed the original instance in time.

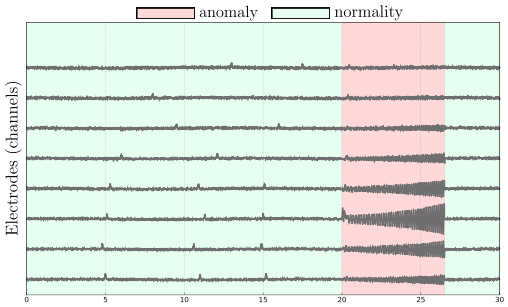

(a) EEG normal phases vs abnormal ones.

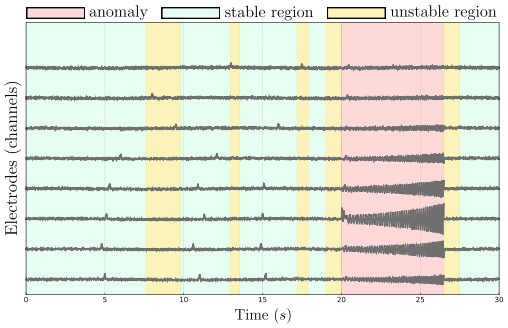

(b) CORTEX identifies, for each anomalous data point at time t, robust (i.e., stable) and normal counterfactual regions at time $< t$.

Figure 2: EEG has electrodes (channels) that record electrical impulses from specific brain regions over time. This can be represented as a multivariate time series. An epileptic event in EEG occurs when a population of cortical neurons (in our case, a combination of channels) fires hypersynchronously, leading to sudden spikes, sharp waves, or rhythmic discharges. These can appear interictally (isolated spikes) or ictally (sustained, evolving patterns).

Since the hard constraint in Equation (2) may occasionally yield no feasible solution, we also consider a relaxed formulation in which temporal instability is penalized rather than enforced:

$$\underset{\substack{G_{t_j} \in \{\mathcal{G}\}_{<t_i} \\ \Phi(G_{t_j}) \neq \Phi(G_{t_i})}}{\arg\min} \quad M(G_{t_i}, G_{t_j}) \; + \; S_{\Phi}(G_{t_j}) \, . \tag{3}$$

3 Related Work

Although our work focuses on counterfactual explanations for multivariate EEG time series modeled as dynamic graphs, we include methods for time series and static graphs for completeness purposes.

Time Series Counterfactual Explainers (TSCEs). Most counterfactual explanation methods are not designed for time series data. Recent approaches aim to fill this gap. For instance, Ates et al. (2021) generate counterfactuals by replacing entire features with those from distractor samples, optimizing for class change and minimal alteration, though this overlooks temporal dependencies. To address this, Delaney et al. (2021) propose an iterative, nearest-neighbor-based method that balances plausibility and sparsity. Yamaguchi et al. (2024) introduce "deviation intervals", restricting changes to decision-critical time regions for greater temporal focus and interpretability. Despite these advances, most time series methods treat inputs as flat vectors, ignoring their spatio-temporal structure or allowing non-actionable modifications to past inputs.

Graph Counterfactual Explainers (GCEs). Most existing counterfactual explainers focus on static graphs. These approaches (Abrate & Bonchi, 2021; Bajaj et al., 2021; Cai et al., 2025; Lucic et al., 2022; Ma et al., 2022; Nguyen et al., 2022; Numeroso & Bacciu, 2021; Prado-Romero et al., 2024a; Prenkaj et al., 2025; Sun et al., 2021; Tan et al., 2022; Wellawatte et al., 2022; Wu et al., 2021) typically perturb the graph minimally (add/remove edges and feature alteration). Search-based techniques (Liu et al., 2021) instead explore the dataset to find optimal counterfactuals based on specific distance metrics (e.g., Graph Edit Distance). However, all these methods overlook time. For a detailed review, see the taxonomy in (Prado-Romero et al., 2024b).

Dynamic GCEs. Counterfactual explanations in temporal graphs remain underexplored, especially in domains where temporal plausibility is critical, such as epileptic seizure detection. Dynamic graphs are classified into Discrete-Time Dynamic Graphs (DTDGs) and Continuous-Time Dynamic Graphs (CTDGs) (Kazemi et al., 2020). While CTDGs offer fine-grained resolution, their irregular event streams make counterfactual generation particularly challenging. CoDy (Qu et al., 2025) uses a search-based approach with Monte Carlo

Tree Search and temporally aware heuristics, but assumes access to continuous event streams, making it unsuitable for DTDGs. In DTDGs, most explainers rely on windowed snapshots. These include explainers based on surrogate models (He et al., 2022), temporal decomposition (Liu et al., 2024), and feature attribution (Fan et al., 2021), but often fail to ensure semantic similarity and plausibility. Generative models like GRACIE (Prenkaj et al., 2024) improve this by modeling class-conditional distributions over snapshots, but still operate at coarse granularity. Generating fine-grained, plausible counterfactuals at the level of individual time steps, without relying on smoothed or aggregated views, remains an open challenge, which we address in this paper.

3.1 Challenges and Gaps in SoTA

TSCEs. Most TSCEs perturb raw input features or limit changes to learned deviation intervals, often ignoring inter-feature dependencies (Ates et al., 2021; Delaney et al., 2021; Yamaguchi et al., 2024). They also allow direct modifications to past data points, an unrealistic assumption in domains where past states are immutable. Instead, we select temporally robust, structurally coherent past instances as counterfactuals, ensuring both plausibility and validity.

Static GCEs. While the explainers in this category capture relational dependencies, they lack temporal awareness and therefore offer limited utility in dynamic settings. We overcome this by treating the system as a sequence of graph snapshots and generating timestamp-level counterfactuals that capture both spatial and temporal structure.

Dynamic GCEs. Dynamic GCEs better reflect evolving systems but often target CTDGs or use windowed aggregation in DTDGs, yielding global temporal (Qu et al., 2025) or coarse-grained explanations (Prenkaj et al., 2024). Such approaches are ill-suited for settings requiring fine temporal resolution. Our method instead operates at per-timestamp granularity (i.e., DTDG with window length one), identifying robust, real past observations as counterfactuals and enabling localized, plausible explanations without temporal smoothing.

4 Context

Let us contextualize the scenario we are dealing with to ensure the reader understands what normality and anomaly in EEG multivariate time series means, and why robust counterfactuals are preferred over mere valid ones. EEG signals are collected from multiple electrodes across different brain regions, measuring electrical activity. Each channel records the potential difference between a pair of electrodes, and the values collected over time constitute the features of the multivariate time series. We consider a binary classification problem: normal (no epilepsy) versus abnormal (epilepsy) condition (see Figure 2a).[2] Our focus is on providing recourse for anomalous phases – that is, identifying the changes required to terminate hypersynchronous neuronal firing – rather than on the transitions from normal to abnormal states. This is motivated by neuroscience and clinical evidence showing that seizures often self-terminate through specific network- and cellular-scale mechanisms, and that interventions aimed at terminating seizures (e.g., closed-loop stimulation) are a major clinical objective (Kramer et al., 2012; Jiruska et al., 2013; Khambhati et al., 2015; Merelli et al., 2016; Connolly et al., 2024). Counterfactual recourse prescribing how to exit the anomalous state is therefore particularly relevant.

In our setting, this multivariate time series at each time t_i gets transformed into a time graph G_{t_i}, where nodes represent channels and the adjacency matrix encodes cross-correlations between channels over a sliding window, following prior work on GNNs for EEG and time series data (Tian & Zhang, 2025; Abadal et al., 2025; Corradini et al., 2026) (see Section B for details). Rather than optimizing for Equation (1) at each t_i in the anomalous phase to simply find another graph G_{t_j} such that $\Phi(G_{t_i}) \neq \Phi(G_{t_j})$, we aim to identify a robust counterfactual that is likely to remain in the normal condition, as defined in Equation (3). Indeed, if we were to select G_{t_j} immediately preceding an anomalous phase, we would obtain a valid counterfactual;

[2] Although abnormal events in EEG are rare, making classification potentially unbalanced, we can mitigate this by sampling the channels during normal phases at different frequencies (e.g., 256Hz instead of 512Hz) and downsampling the series from the source, yielding a balanced dataset.

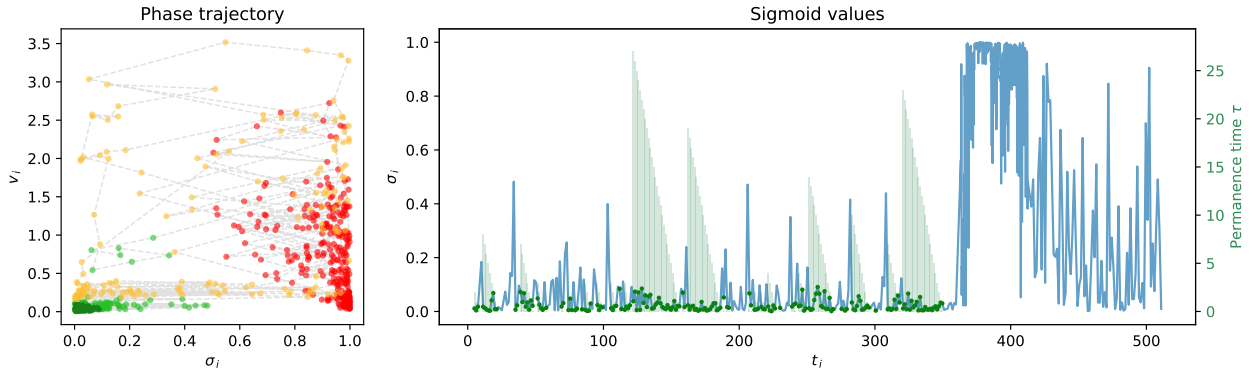

Figure 3: (left) Sigmoid phase trajectory, colored by the oracle classification within the time window of length w (green if all points in the window belong to class 0; red if all belong to class 1; and yellow if the classification changes within the window, indicating transition regions). Darker green points indicate elements in $\mathcal{G}'_q$. (right) Sigmoid values over time, along with points in $\mathcal{G}'_q$ (green points) and their residual permanence times τ. Example from record `chb03_01`.

however, this approach lacks robustness: advancing time from that state, the system typically returns to the anomalous regime, making G_{t_j} unsuitable in terms of robustness and plausibility (Guidotti, 2022). CORTEX, instead, distributes counterfactuals into "stable" and "unstable" regions, and restricts the search to those unlikely to return to the anomalous condition in the near future, which are considered temporally robust (see Figure 2b) w.r.t. Φ's outcome.

5 Methodology

Here, we introduce our novel search-based explainer, COunterfactual Reasoning for Temporal EXplanations (CORTEX), that accounts for the relationship among feature, time, and space by modeling multivariate EEG series as spatio-temporal graphs. In our setting, each time step t_i of the time series is mapped to a graph G_{t_i} whose nodes correspond to features (here, EEG channels) and edges encode their relationship (here, cross-correlation over a temporal window), following standard practices in the GNN literature for time series data (Corradini et al., 2026). On top of this representation, CORTEX produces counterfactuals – see Section A for an algorithmic overview. Recall that we want to ensure the validity and plausibility of the counterfactuals. Therefore, instead of sampling from a learned latent distribution – see Ma et al. (2022); Prado-Romero et al. (2024a); Prenkaj et al. (2025) among others – we directly search for robust counterfactuals among past observations in the dataset.

Robust Counterfactual Identification. Let $\sigma : \mathcal{G} \to [0, 1]$ be the function that assigns a continuous score to each graph G_{t_i} such that $\Phi(G_{t_i}) = \mathbf{1}[\sigma(G_{t_i}) \geq \theta]$ for a threshold $\theta \in [0, 1]$. For simplicity, we write $\sigma_i = \sigma(G_{t_i})$.

A straightforward way to quantify the temporal robustness of the classification is to track the score σ over time. In more detail, given a graph G_{t_i}, we calculate (σ_i, v_i), where σ_i is the sigmoid value associated with $\Phi(G_{t_i})$, and v_i is the sigmoid oscillation velocity calculated over the next w time steps (ensuring it remains within the series length T):

$$v_i = \frac{\sum_{j=0}^{w-1} \left| \sigma_{\min(i+j+1,T)} - \sigma_{\min(i+j,T)} \right|}{t_{\min(i+w,T)} - t_i}, \tag{4}$$

where the denominator accounts for different sampling rates between the classes.[2] High values of v_i correspond to greater amplitudes in the oscillations, which can lead to local instability of the predicted class of G_{t_i} in the immediately succeeding time steps (i.e., lack of temporal robustness). Note that this computation does not violate causality, because all values used to compute v_i have already been observed in the time series.

Given a graph G_{t_i} s.t. $\Phi(G_{t_i}) = 1$ (abnormal), we want to find counterfactuals G_{t_j} with a low output-velocity combination. One can map each (σ_i, v_i) point into a output-velocity plot (see Figure 3 (left)). Note that the ideal position for G_{t_j} is at $(0, 0)$, since the sigmoid value indicates that Φ classifies G_{t_j} as normal with a high score, and the velocity shows that G_{t_j} has no risk of crossing Φ's decision boundary in the near future (up to w time steps). Alas, in reality, it is unlikely that all counterfactuals G_{t_j} are in $(0, 0)$. Thus, we rank them according to their Euclidean distance $\delta_j = \sqrt{\sigma_j^2 + v_j^2}$ from $(0, 0)$. Given the set of valid counterfactual candidates $\mathcal{G}'$ for G_{t_i}:

$$\mathcal{G}' = \left\{ (G_{t_j}, \delta_j) \mid \Phi(G_{t_j}) \neq \Phi(G_{t_i}) \;\; \wedge \;\; \delta_j = \sqrt{\sigma_j^2 + v_j^2} \right\}, \tag{5}$$

we sort all its elements in ascending order according to δ_j and select the top $q\%$ to form the subset $\mathcal{G}'_q$:

$$(G_{t_j}, \delta_j) \in \mathcal{G}'_q \iff (G_{t_j}, \delta_j) \in \mathcal{G}' \;\; \wedge \;\; \text{rank}^{\uparrow}_{\delta}\big((G_{t_j}, \delta_j), \mathcal{G}'\big) \leq \lceil q \cdot |\mathcal{G}'| \rceil \,, \tag{6}$$

where $\text{rank}^{\uparrow}_{\delta}\big((G_{t_j}, \delta_j), \mathcal{G}'\big)$ is the 1-based rank of δ_j in ascending order within $\mathcal{G}'$ (i.e., smallest δ gets 1), and $\lceil q \cdot |\mathcal{G}'| \rceil$ gives the top $q\%$ cutoff. We refer the reader to Section B for details on w in Equation (4) and q in Equation (6). Similarly to Equation (2), $\{\mathcal{G}'\}_{<t_i}$ and $\{\mathcal{G}'_q\}_{<t_i}$ denote the sets of valid and plausible counterfactuals for G_{t_i} that occur prior to time t_i in $\mathcal{G}'$ and $\mathcal{G}'_q$, respectively. In what follows, we abuse the notation, and use $G_{t_j} \in \{\mathcal{G}'\}_{<t_i}$ to indicate that G_{t_j} belongs to $\{\mathcal{G}'\}_{<t_i}$ instead of $(G_{t_j}, \delta_j) \in \{\mathcal{G}'\}_{<t_i}$ for readability purposes. The same applies for $\{\mathcal{G}'_q\}_{<t_i}$.[3]

Multi-Objective Selection Criterion. Once we obtain $\mathcal{G}'_q \subset \mathcal{G}$, we search for the best counterfactuals by minimizing a metric function $M : \mathcal{G} \times \mathcal{G} \to \mathbb{R}_{\geq 0}$. Given G_{t_i}, CORTEX searches over all $G_{t_j} \in \{\mathcal{G}'_q\}_{<t_i}$ and optimizes M containing three components: (1) the dissimilarity between G_{t_i} and G_{t_j}, (2) their temporal distance, and (3) the robustness of G_{t_j}.

(1) Dissimilarity Metric. We define M_α as the Frobenius norm of the difference between the product of the Laplacians of G_{t_i} and G_{t_j} and their node feature matrices:

$$M_\alpha(G_{t_i}, G_{t_j}) = \left\| L_{t_i} X_{t_i} - L_{t_j} X_{t_j} \right\|_F \,, \tag{7}$$

where $L_{t_i} \in \mathbb{R}^{|n_{t_i}| \times |n_{t_i}|}$ is the normalized Laplacian matrix of graph G_{t_i} defined as $L_{t_i} = I - {D_{t_i}}^{-1/2} A_{t_i} {D_{t_i}}^{-1/2}$ s.t. $D_{t_i} \in \mathbb{N}^{n_{t_i} \times n_{t_i}}$ is the diagonal degree matrix of G_{t_i}, and $I \in \mathbb{R}^{n_{t_i} \times n_{t_i}}$ is the identity matrix. The attentive reader would notice that Equation (7) is defined only if $n_{t_i} = n_{t_j}$ and the nodes are considered in the same order. This condition holds in our scenario because each node consistently represents the same feature across the multivariate time series (see also Section 6.2). Note also that M_α does not rely on Φ for its computation; this is because distances between oracle embeddings would reflect differences in class representations rather than single graph dissimilarities. Indeed, Φ tends to map instances of the same class close together in the embedding space, even if the graphs differ significantly. As a result, oracle-based distances would be biased towards class semantics and overlook structural graph differences.

(2) Temporal Distance. We also want to favor counterfactuals in $\{\mathcal{G}'_q\}_{<t_i}$ that are temporally close to the original instance. Thus, we define M_β as the quadratic difference between t_i and t_j:

$$M_\beta(G_{t_i}, G_{t_j}) = (t_i - t_j)^2 \,. \tag{8}$$

We chose a quadratic form to heavily penalize graphs further away in time. However, a study of other penalization function (e.g., linear) is left for future work.

(3) Temporal Robustness. For each $G_{t_j} \in \mathcal{G}'_q$, we define the residual permanence time τ_j as the number of consecutive time steps during which the sequence remains in $\mathcal{G}'_q$. Formally, let the permanence time τ_j for $G_{t_j} \in \mathcal{G}'_q$ be:

$$\tau_j = \max\{h \in \mathbb{N} \mid G_{t_{j+h}} \in \mathcal{G}'_q\} \,. \tag{9}$$

[3] If $\{\mathcal{G}'\}_{<t_i} = \varnothing$ – i.e., either no possible counterfactuals due to (rare) poor training of Φ, or every counterfactual is in the future – a valid counterfactual cannot be produced. In such cases, the original instance is returned.

Table 1: CORTEX vs SoTA in terms of validity (↑). Best results in **bold**, second-best underlined. CORTEX has a 2.73× improvement over the second-best performing method across the board.

	chb01_03	chb01_04	chb01_15	chb01_16	chb01_18	chb01_21	chb01_26	chb03_01	chb03_02	chb03_03	chb03_04	chb03_34	chb03_35	chb03_36	chb10_12
OBS	0.1037	0.3255	0.1724	0.4848	0.5325	0.2076	0.4122	0.3227	0.1629	0.2294	0.3008	0.3501	0.2365	0.2100	0.4468
DDBS	0.0469	0.1693	0.0517	0.3384	0.4431	0.0506	0.1888	0.1493	0.0451	0.1322	0.1303	0.1289	0.0468	0.0787	0.1835
GNN-MOExp	0.0617	0.1745	0.0690	0.1433	0.1341	0.0532	0.0798	0.1493	0.0902	0.1596	0.2105	0.2577	0.1034	0.1391	0.0718
CORTEX	**1.0000**	**1.0000**	**1.0000**	**1.0000**	**1.0000**	**1.0000**	**1.0000**	**1.0000**	**1.0000**	**1.0000**	**1.0000**	**1.0000**	**1.0000**	**1.0000**	**1.0000**

	chb10_20	chb10_27	chb10_30	chb10_38	chb10_89	PN00_1	PN00_2	PN00_4	PN00_5	PN06_2	PN06_3	PN06_4	PN06_5	PN14_1	PN14_2	PN14_4
OBS	0.1969	0.1028	0.4083	0.1813	0.3307	0.9599	0.5417	0.6566	0.2610	0.5257	0.5923	0.3764	0.7695	0.5311	0.1610	0.0471
DDBS	0.0787	0.0401	0.1705	0.0879	0.1601	0.9091	0.4083	0.5412	0.1951	0.4562	0.4962	0.2802	0.7366	0.3672	0.1384	0.0443
GNN-MOExp	0.0997	0.0952	0.1163	0.1071	0.2021	0.9465	0.9028	0.8819	0.4176	0.4350	0.5231	0.5604	0.3745	0.6045	0.2571	0.0886
CORTEX	**1.0000**	**1.0000**	**1.0000**	**1.0000**	**1.0000**	**1.0000**	**1.0000**	**1.0000**	**1.0000**	**1.0000**	**1.0000**	**1.0000**	**1.0000**	**1.0000**	**1.0000**	**1.0000**

Thus, τ_j counts the length of the maximal contiguous block $G_{t_{j+1}}, G_{t_{j+2}}, \ldots$ that lies entirely in $\mathcal{G}'_q$. We then normalize τ_j into an instability score M_γ, mapping the largest permanence to 0 (most robust) and the smallest permanence to 1 (least robust), with intermediate values scaled linearly between 0 and 1. Formally, for all G_{t_j} with (finite) permanence time τ_j we define

$$M_\gamma(G_{t_j}) \;=\; \frac{\tau_{\max} - \tau_j}{\tau_{\max} - \tau_{\min}}\,, \tag{10}$$

where $\tau_{\max} = \max\{\tau_j\}$ and $\tau_{\min} = \min\{\tau_j\}$ $\forall G_{t_j} \in \mathcal{G}'_q$ (by construction, $\tau_{\min} = 0$). If $\tau_{\max} = 0$, the set $\mathcal{G}'_q$ only contains isolated robust counterfactual candidates. In this case, to avoid division by zero in Equation (10), we set $M_\gamma(G_j) \equiv 1$. Note how Equation (10) subsumes the role of S_Φ in Equation (3) since it associates every graph with an instability score over the top-q^{th} most robust percentile of counterfactuals in $\mathcal{G}'_q$. We illustrate the permanence time with the shaded areas in Figure 3 (right).

CORTEX optimizes Equation (11) to find a counterfactual given a graph G_{t_i}, where each term is first normalized in $[0, 1]$ across all candidates in $\{\mathcal{G}'_q\}_{<t_i}$ to balance their contributions to the overall metric:

$$\underset{G_{t_j} \in \{\mathcal{G}'_q\}_{<t_i}}{\arg\min} \underbrace{M_\alpha(G_{t_i}, G_{t_j}) + M_\beta(G_{t_i}, G_{t_j})}_{M \text{ in Eq.(3)}} + \underbrace{M_\gamma(G_{t_j})}_{S_\Phi \text{ in Eq.(3)}}\,. \tag{11}$$

Note that one can also produce the top-k counterfactuals rather than the top-1 as described above.

Satisfied Counterfactuality Properties. CORTEX satisfies all desiderata in (Guidotti, 2022) (besides actionability and causality, as justified in Section 2). Validity and plausibility hold since the search for counterfactuals is done over $\{\mathcal{G}'_q\}_{<t_i}$ which, by construction, should contain valid and plausible ones – see Equations (5) and (6). Proximity is enforced via M_α that accounts for both topology and node features. Finally, we guarantee temporal robustness by selecting robust candidates in $\{\mathcal{G}'_q\}_{<t_i}$ (see Figure 3 (left)) and further reinforce it through M_γ.

6 Experiments

6.1 Datasets

PhysioNet CHB-MIT Scalp EEG (Shoeb, 2010) contains EEGs from 22 pediatric patients sampled at 256 Hz. *PhysioNet Siena Scalp EEG* (Detti, 2020) has 14 adult patient EEGs sampled at 512 Hz. We select three patients from each dataset having the highest number of recordings and seizures: `chb01`, `chb03`, `chb10`, `PN00`, `PN06`, and `PN14`. For each patient, we use all recordings with seizure events that share the same set of EEG channels to ensure data consistency and maximize the information used. Here we treat the EEG series of each patient as a separate dataset, resulting in a total of 31 recordings. Each recording contains graphs in time, where nodes correspond to EEG channels, and edges among them encode their cross-correlations. The

graphs reflect the spatial configuration of the electrodes and the temporal dynamics of their interactions. We point the reader to Sec. B for a detailed description of how to build these time graphs from the patient recordings.

6.2 Experimental Setup

Oracle training. For each patient, we train a 2-layer GCN end-to-end on all their EEG recordings to predict the label of each graph G_{t_i} at its time t_i. We are aware that various GNN architectures, including spatio-temporal models (Corradini et al., 2026), can be used. However, we refrain from committing to a specific design, as CORTEX is a post-hoc explainer and a full architectural comparison of the oracle is outside the scope of this work. Once trained, Φ acts as a black-box oracle that provides predictions used throughout the counterfactual generation pipeline.

Baselines. We compare CORTEX[4] with two heuristic-based explainers – i.e., OBS and DDBS (Abrate & Bonchi, 2021) – and a hybrid-based (search+heurstic) explainer GNN-MOExp (Liu et al., 2021). DDBS finds counterfactuals by filtering edges according to their probability of appearing in graphs of a given class. In our experiments, we adapt DDBS to compute these probabilities using only past instances, thereby preventing the use of illegitimate future information in time series settings.

We noticed that learning-based explainers (e.g., Ma et al. (2022)) are unsuitable in our scenario because most recordings described above have a single anomalous phase. Since learning-based explainers require a mandatory training process, splitting the time series into train-test portions might produce splits that do not preserve the temporal dependency (i.e., training data in the future, test in the past). In this way, during training these explainers would see the future beforehand and they would not guarantee to produce a counterfactual that is in the past (see the conditions under arg min in Equations (2) and (3)). Hence, we exclude them from our analysis. We also exclude TSCEs from our comparison, they produce explanations by modifying past instances, as they generate explanations by modifying past instances, making their results not directly comparable with CORTEX. In future work, we plan to adapt all these explainers to time graphs. Recall that CORTEX belongs to the class of DTDG dynamic explainers, and the only work in the literature is GRACIE (Prenkaj et al., 2024). However, GRACIE requires to create two VGAE "experts" that represent the two classes in EEG at time t_0. Because at t_0 for each recording we only have one graph, GRACIE fails to learn these representations. Hence, it is a meaningless competitor in our scenario.

6.3 Results and Analysis

CORTEX outperforms SoTA in terms of validity (2.73× better) and fidelity (5.32× better). Tables 1 and 2 report average validity and fidelity of CORTEX and SoTA methods across all 31 EEG recordings. CORTEX consistently achieves the highest scores, outperforming all SoTA models across the board. Errors occur only when explaining instances misclassified by the oracle (i.e., when explaining false negatives) for which CORTEX has no valid candidate in $\{\mathcal{G}'_q\}_{<t_i}$. Contrarily, SoTA models primarily focus on perturbing the original instance while minimizing dissimilarity, but this often comes at the cost of validity.

Including $\mathbf{M}_\beta$ and $\mathbf{M}_\gamma$ in Equation (11) has little effect on dissimilarity $\mathbf{M}_\alpha$. Table 3 shows the impact of $\{\mathcal{G}'\}_{<t_i}$ vs $\{\mathcal{G}'_q\}_{<t_i}$, as well as the temporal distance and robustness terms of Equation (11) on the top-5 counterfactuals on `chb03_01`. Note that for explainers performing searches over $\{\mathcal{G}'\}_{<t_i}$, the term M_γ is not defined.

The values of M_α remain consistent across the board. M_β makes CORTEX choose counterfactuals closer in time to the original graph, with small std (see $\sqrt{M_\beta}$) indicating that the counterfactuals are more similar to each other w.r.t. the underlying dynamic conditions. Notice that M_β and M_γ are specular optimization metrics (see row 5 and 6). M_γ prefers counterfactuals that stay longer in "stable" regions – i.e., the left-most data point in a stable region is preferred but it is also further away from the original instance than the right-most one as shown in Figure 3 (right). M_β penalizes this temporal distance. However, when both are included (last row) there is a staggering trade-off where M_β improves of 62.93% whereas M_γ is just reduced of 0.08 points. Notice also that when both these metrics are included, the std of M_β is the lowest among

[4]Source code: `https://anonymous.4open.science/r/CORTEX/`

Table 2: CORTEX vs SoTA in terms of fidelity (↑). Best results in **bold**, second-best underlined. CORTEX has a 5.32× improvement over the SoTA across the board.

	chb01_03	chb01_04	chb01_15	chb01_16	chb01_18	chb01_21	chb01_26	chb03_01	chb03_02	chb03_03	chb03_04	chb03_34	chb03_35	chb03_36	chb10_12
OBS	0.0439	0.1326	0.0719	0.1550	0.1101	0.0884	0.1731	0.1381	0.0747	0.0818	0.1296	0.1415	0.0964	0.0828	0.1933
DDBS	0.0179	0.0705	0.0315	0.1070	0.0835	0.0267	0.0879	0.0716	0.0237	0.0481	0.0585	0.0490	0.0229	0.0284	0.0785
GNN-MOExp	0.0499	0.0951	0.0455	-0.0254	-0.1567	0.0300	0.0233	0.0901	0.0877	0.0964	0.1571	0.1947	0.0631	0.0960	0.0030
CORTEX	**0.9258**	**0.8910**	**0.4750**	**0.7263**	**0.6106**	**0.9259**	**0.8700**	**0.8953**	**0.9372**	**0.9159**	**0.9454**	**0.9147**	**0.9178**	**0.9261**	**0.8672**

	chb10_20	chb10_27	chb10_30	chb10_38	chb10_89	PN00_1	PN00_2	PN00_4	PN00_5	PN06_2	PN06_3	PN06_4	PN06_5	PN14_1	PN14_2	PN14_4
OBS	0.0766	0.0449	0.1853	0.0966	0.1412	0.4405	0.1918	0.2346	0.0998	0.1095	0.1001	0.0862	0.1684	0.1801	0.0489	0.0143
DDBS	0.0314	0.0186	0.0824	0.0500	0.0706	0.4080	0.1323	0.1781	0.0698	0.0877	0.0747	0.0562	0.1522	0.1270	0.0433	0.0121
GNN-MOExp	0.0615	0.0748	0.0580	0.0828	0.1310	**0.8729**	**0.7583**	**0.7435**	0.3203	0.1724	0.1698	0.2953	0.0485	0.3868	0.2107	0.0683
CORTEX	**0.9285**	**0.9067**	**0.9057**	**0.7965**	**0.8740**	0.8202	0.6686	0.6095	**0.7912**	**0.5546**	**0.3643**	**0.4710**	**0.5368**	**0.7235**	**0.7713**	**0.8753**

Table 3: Study of variants of Equation (11) and the search space. We show average and std of M_α, $\sqrt{M_\beta}$, and M_γ computed over the top-5 counterfactuals for `chb03_01` (oracle accuracy: 0.9336). The components of all optimization variants are normalized in $[0, 1]$ as described in Equation (11). All values are computed only on the explanations for the correctly classified instances (i.e., true positives). Last row is CORTEX.

Variant	Search Space	M_α (↓)	$\sqrt{M_\beta}$ (↓)	M_γ (↓)
$M = M_\alpha + M_\beta$	$\{\mathcal{G}'_q\}_{<t_i}$	0.439 ± 0.004	61.787 ± 16.309	0.714 ± 0.203
$M = M_\alpha + M_\beta$	$\{\mathcal{G}'\}_{<t_i}$	0.419 ± 0.011	39.282 ± 10.132	—
$M = M_\alpha$	$\{\mathcal{G}'_q\}_{<t_i}$	0.433 ± 0.003	189.886 ± 86.495	0.782 ± 0.187
$M = M_\alpha$	$\{\mathcal{G}'\}_{<t_i}$	0.430 ± 0.004	182.502 ± 88.909	—
$M = M_\alpha + M_\gamma$	$\{\mathcal{G}'_q\}_{<t_i}$	0.451 ± 0.008	179.553 ± 91.993	0.150 ± 0.062
$M = M_\alpha + M_\beta + M_\gamma$	$\{\mathcal{G}'_q\}_{<t_i}$	0.451 ± 0.006	66.560 ± 3.980	0.230 ± 0.065

all variants. Finally, optimizing also for M_γ has the largest gain (compare rows 1 and 3 with 5 and 6). As expected from Equation (3) and Section 5, the robustness of counterfactuals clearly ameliorates their quality (+67.8% in M_γ) at only a small decreased temporal distance (−7.17% in $\sqrt{M_\beta}$) and increased dissimilarity (+4.88% in M_α) – compare row 1 with last.

6.4 Discussion: Plausibility vs Dissimilarity

By design, CORTEX achieves zero implausibility by restricting the counterfactual search to robust instances within the dataset, effectively producing counterfactuals that have already been observed. Contrarily, OBS and DDBS generate explanations by modifying the original graph. As a consequence, the counterfactuals remain close to the original instance (low dissimilarity) rather than truly reflecting the characteristics of graphs that Φ would classify as normal (resulting in high implausibility). GNN-MOExp does not enforce the same nodes between the original and counterfactual graphs, resulting in an undefined implausibility score (see Equation (15)).

Notably, when implausibility is high, dissimilarity becomes irrelevant, since such counterfactuals are inherently unsuitable regardless of their proximity to the original graph. In other words, we argue that plausibility is a necessary condition: *only counterfactuals with low implausibility should be considered, and only then, dissimilarity becomes a meaningful criterion for further selection*. Even if OBS and DDBS show lower dissimilarity scores due to generating counterfactuals with identical node features and binary adjacency matrices, this alone does not guarantee explanation quality if plausibility is not satisfied. See Section D for details on the implausibility-dissimilarity relationship among the explainers.

7 Conclusion

We introduced CORTEX, a novel search-based explainer that finds reliable and robust counterfactuals for multivariate EEG series represented as spatio-temporal graphs. By moving beyond the conventional focus on minimizing feature perturbations, CORTEX explicitly addresses the critical needs of dynamic, high-stakes domains by proposing temporal robustness – i.e., ensuring the suggested recourse remains valid over subsequent time steps – as a new desideratum for counterfactuals. Evaluated on EEG-based seizure detection, CORTEX significantly outperformed existing SoTA, achieving a 2.73× improvement in validity and a 5.32× improvement in fidelity, while crucially maintaining zero implausibility.

Building upon these foundations, future work directions include exploring alternative penalization functions for the temporal distance metric to better calibrate the importance of time, and generalizing the method to handle a wider variety of dynamic graph structures. Most importantly, integrating explicit notions of actionability and causality will be essential to further enhance the clinical utility and trustworthiness of CORTEX for expert practitioners.

References

Sergi Abadal, Pablo Galván, Alberto Mármol, Nadia Mammone, Cosimo Ieracitano, Michele Lo Giudice, Alessandro Salvini, and Francesco Carlo Morabito. Graph neural networks for electroencephalogram analysis: Alzheimer's disease and epilepsy use cases. *Neural Networks*, 181:106792, 2025. ISSN 0893-6080. doi: https://doi.org/10.1016/j.neunet.2024.106792. URL `https://www.sciencedirect.com/science/article/pii/S0893608024007160`.

Carlo Abrate and Francesco Bonchi. Counterfactual graphs for explainable classification of brain networks. In *Proceedings of the 27th ACM SIGKDD Conference on Knowledge Discovery & Data Mining*, KDD '21, pp. 2495–2504, New York, NY, USA, 2021. Association for Computing Machinery. ISBN 9781450383325. doi: 10.1145/3447548.3467154. URL `https://doi.org/10.1145/3447548.3467154`.

Emre Ates, Burak Aksar, Vitus J. Leung, and Ayse K. Coskun. Counterfactual explanations for multivariate time series. In *2021 International Conference on Applied Artificial Intelligence (ICAPAI)*, pp. 1–8, 2021. doi: 10.1109/ICAPAI49758.2021.9462056.

Mohit Bajaj, Lingyang Chu, Zi Yu Xue, Jian Pei, Lanjun Wang, Peter Cho-Ho Lam, and Yong Zhang. Robust counterfactual explanations on graph neural networks. *Advances in Neural Information Processing Systems*, 34:5644–5655, 2021.

Ruichu Cai, Yuxuan Zhu, Xuexin Chen, Yuan Fang, Min Wu, Jie Qiao, and Zhifeng Hao. On the probability of necessity and sufficiency of explaining graph neural networks: A lower bound optimization approach. *Neural Networks*, 184:107065, 2025.

Mark J. Connolly, Sujin Jiang, Lim C. Samuel, Claire-Anne Gutekunst, Robert E. Gross, and Annaelle Devergnas. Seizure onset and offset pattern determine the entrainment of the cortex and substantia nigra in the nonhuman primate model of focal temporal lobe seizures. *Plos one*, 19(8):e0307906, 2024.

Flavio Corradini, Flavio Gerosa, Marco Gori, Carlo Lucheroni, Marco Piangerelli, and Martina Zannotti. A systematic literature review of spatio-temporal graph neural network models for time series forecasting and classification. *Neural Networks*, 195:108269, 2026. ISSN 0893-6080. doi: https://doi.org/10.1016/j.neunet.2025.108269. URL `https://www.sciencedirect.com/science/article/pii/S0893608025011505`.

Eoin Delaney, Derek Greene, and Mark T. Keane. Instance-based counterfactual explanations for time series classification. In *Case-Based Reasoning Research and Development: 29th International Conference, ICCBR 2021, Salamanca, Spain, September 13–16, 2021, Proceedings*, pp. 32–47, Berlin, Heidelberg, 2021. Springer-Verlag. ISBN 978-3-030-86956-4. doi: 10.1007/978-3-030-86957-1_3. URL `https://doi.org/10.1007/978-3-030-86957-1_3`.

Paolo Detti. Siena scalp eeg database, 2020. URL `https://physionet.org/content/siena-scalp-eeg/1.0.0/`.

Yucai Fan, Yuhang Yao, and Carlee Joe-Wong. Gcn-se: Attention as explainability for node classification in dynamic graphs. In *2021 IEEE International Conference on Data Mining (ICDM)*, pp. 1060–1065. IEEE, 2021.

R. Guidotti. Counterfactual explanations and how to find them: literature review and benchmarking. *Data Mining and Knowledge Discovery*, pp. 1–55, 2022.

Wenchong He, Minh N Vu, Zhe Jiang, and My T Thai. An explainer for temporal graph neural networks. In *GLOBECOM 2022-2022 IEEE Global Communications Conference*, pp. 6384–6389. IEEE, 2022.

Junqi Jiang, Francesco Leofante, Antonio Rago, and Francesca Toni. Robust counterfactual explanations in machine learning: a survey. In *Proceedings of the Thirty-Third International Joint Conference on Artificial Intelligence*, IJCAI '24, 2024. ISBN 978-1-956792-04-1. doi: 10.24963/ijcai.2024/894. URL `https://doi.org/10.24963/ijcai.2024/894`.

Premysl Jiruska, Marco De Curtis, John G. R. Jefferys, Catherine A. Schevon, Steven J. Schiff, and Kaspar Schindler. Synchronization and desynchronization in epilepsy: controversies and hypotheses. *The Journal of physiology*, 591(4):787–797, 2013.

Seyed Mehran Kazemi, Rishab Goel, Kshitij Jain, Ivan Kobyzev, Akshay Sethi, Peter Forsyth, and Pascal Poupart. Representation learning for dynamic graphs: A survey. *Journal of Machine Learning Research*, 21(70):1–73, 2020.

Ankit N. Khambhati, Kathryn A. Davis, Brian S. Oommen, Stephanie H. Chen, Timothy H. Lucas, Brian Litt, and Danielle S. Bassett. Dynamic network drivers of seizure generation, propagation and termination in human neocortical epilepsy. *PLoS computational biology*, 11(12):e1004608, 2015.

Thomas N. Kipf and Max Welling. Semi-Supervised Classification with Graph Convolutional Networks. In *Proceedings of the 5th International Conference on Learning Representations*, ICLR '17, 2017. URL `https://openreview.net/forum?id=SJU4ayYgl`.

Mark A. Kramer, Wilson Truccolo, Uri T. Eden, Kyle Q. Lepage, Leigh R. Hochberg, Emad N. Eskandar, Joseph R. Madsen, Jong W. Lee, Atul Maheshwari, Eric Halgren, Catherine J. Chu, and Sydney S. Cash. Human seizures self-terminate across spatial scales via a critical transition. *Proceedings of the National Academy of Sciences*, 109(51):21116–21121, 2012.

Yazheng Liu, Xi Zhang, and Sihong Xie. A differential geometric view and explainability of gnn on evolving graphs. *arXiv preprint arXiv:2403.06425*, 2024.

Yifei Liu, Chao Chen, Yazheng Liu, Xi Zhang, and Sihong Xie. Multi-objective explanations of gnn predictions. In *2021 IEEE International Conference on Data Mining (ICDM)*, pp. 409–418. IEEE, 2021.

Ana Lucic, Maartje Ter Hoeve, Gabriele Tolomei, Maarten De Rijke, and Fabrizio Silvestri. Cf-gnnexplainer: Counterfactual explanations for graph neural networks. In *Int. Conf. on AI and Statistics*, pp. 4499–4511. PMLR, 2022.

Jing Ma, Ruocheng Guo, Saumitra Mishra, Aidong Zhang, and Jundong Li. CLEAR: Generative counterfactual explanations on graphs. In Alice H. Oh, Alekh Agarwal, Danielle Belgrave, and Kyunghyun Cho (eds.), *Advances in Neural Information Processing Systems*, 2022. URL `https://openreview.net/forum?id=YR-s5leIvh`.

Emanuela Merelli, Marco Piangerelli, Matteo Rucco, and Daniele Toller. A topological approach for multivariate time series characterization: the epileptic brain. In *Proceedings of the 9th EAI International Conference on Bio-inspired Information and Communications Technologies (BICT)*. ACM, May 2016. doi: 10.4108/eai.3-12-2015.2262525.

Tri Minh Nguyen, Thomas P. Quinn, Thin Nguyen, and Truyen Tran. Explaining black box drug target prediction through model agnostic counterfactual samples. *IEEE/ACM Transactions on Computational Biology and Bioinformatics*, 2022.

Danilo Numeroso and Davide Bacciu. Meg: Generating molecular counterfactual explanations for deep graph networks. In *2021 International Joint Conference on Neural Networks (IJCNN)*, pp. 1–8. IEEE, 2021.

Mario Alfonso Prado-Romero and Giovanni Stilo. Gretel: Graph counterfactual explanation evaluation framework. In *Proceedings of the 31st ACM International Conference on Information and Knowledge Management*, CIKM '22, New York, NY, USA, 2022. Association for Computing Machinery. ISBN 9781450392365. doi: 10.1145/3511808.3557608.

Mario Alfonso Prado-Romero, Bardh Prenkaj, and Giovanni Stilo. Robust stochastic graph generator for counterfactual explanations. In *Proceedings of the Thirty-Eighth AAAI Conference on Artificial Intelligence and Thirty-Sixth Conference on Innovative Applications of Artificial Intelligence and Fourteenth Symposium on Educational Advances in Artificial Intelligence*, AAAI'24/IAAI'24/EAAI'24. AAAI Press, 2024a. ISBN 978-1-57735-887-9. doi: 10.1609/aaai.v38i19.30149. URL https://doi.org/10.1609/aaai.v38i19.30149.

Mario Alfonso Prado-Romero, Bardh Prenkaj, Giovanni Stilo, and Fosca Giannotti. A survey on graph counterfactual explanations: Definitions, methods, evaluation, and research challenges. *ACM Comput. Surv.*, 56(7), April 2024b. ISSN 0360-0300. doi: 10.1145/3618105. URL https://doi.org/10.1145/3618105.

Bardh Prenkaj, Mario Villaizán-Vallelado, Tobias Leemann, and Gjergji Kasneci. Unifying evolution, explanation, and discernment: A generative approach for dynamic graph counterfactuals. In *Proceedings of the 30th ACM SIGKDD Conference on Knowledge Discovery and Data Mining*, pp. 2420–2431, 2024.

Bardh Prenkaj, Efstratios Zaradoukas, and Gjergji Kasneci. Graph inverse style transfer for counterfactual explainability. In *Forty-second International Conference on Machine Learning*, 2025. URL https://openreview.net/forum?id=5Z27aGSgJ4.

Zhan Qu, Daniel Gomm, and Michael Färber. Cody: Counterfactual explainers for dynamic graphs. In *Forty-second International Conference on Machine Learning*, 2025.

Ali Shoeb. Chb-mit scalp eeg database, 2010. URL https://physionet.org/content/chbmit/.

Yi Sun, Abel Valente, Sijia Liu, and Dakuo Wang. Preserve, promote, or attack? gnn explanation via topology perturbation. *arXiv preprint arXiv:2103.13944*, 2021.

Juntao Tan, Shijie Geng, Zuohui Fu, Yingqiang Ge, Shuyuan Xu, Yunqi Li, and Yongfeng Zhang. Learning and evaluating graph neural network explanations based on counterfactual and factual reasoning. In *Proceedings of the ACM Web Conference 2022*, WWW '22, pp. 1018–1027, New York, NY, USA, 2022. Association for Computing Machinery. ISBN 9781450390965. URL https://doi.org/10.1145/3485447.3511948.

Chongrui Tian and Fengbin Zhang. Eeg-based epilepsy detection with graph correlation analysis. *Frontiers in Medicine*, 12, March 2025. ISSN 2296-858X. doi: 10.3389/fmed.2025.1549491. URL http://dx.doi.org/10.3389/fmed.2025.1549491.

Sandra Wachter, Brent Mittelstadt, and Chris Russell. Counterfactual explanations without opening the black box: Automated decisions and the gdpr. *Harv. JL & Tech.*, 31:841, 2017.

Geemi P. Wellawatte, Aditi Seshadri, and Andrew D. White. Model agnostic generation of counterfactual explanations for molecules. *Chemical science*, 13(13):3697–3705, 2022.

Haoran Wu, Wei Chen, Shuang Xu, and Bo Xu. Counterfactual supporting facts extraction for explainable medical record based diagnosis with graph network. In *Proceedings of the 2021 Conference of the North American Chapter of the Association for Computational Linguistics: Human Language Technologies*, pp. 1942–1955, 2021.

Akihiro Yamaguchi, Ken Ueno, Ryusei Shingaki, and Hisashi Kashima. Learning counterfactual explanations with intervals for time-series classification. In *Proceedings of the 33rd ACM International Conference on Information and Knowledge Management*, CIKM '24, pp. 4158–4162, New York, NY, USA, 2024. Association for Computing Machinery. ISBN 9798400704369. doi: 10.1145/3627673.3679952. URL https://doi.org/10.1145/3627673.3679952.

Hao Yuan, Haiyang Yu, Shurui Gui, and Shuiwang Ji. Explainability in graph neural networks: A taxonomic survey. *IEEE Transactions on Pattern Analysis and Machine Intelligence*, 45:5782–5799, 5 2023. ISSN 19393539. doi: 10.1109/TPAMI.2022.3204236.

A Algorithmic Overview

For clarity and completeness, we show the pseudo-code of CORTEX in Algorithm 1.

Algorithm 1 CORTEX

1: **Input:** $\mathcal{G} = \{G_{t_1}, G_{t_2}, \ldots, G_{t_T}\}$; pre-trained oracle $\Phi : \mathcal{G} \to Y$; threshold $0 \leq \theta \leq 1$; $w > 0$, $q > 0$; number of counterfactuals k
2: **Output:** top-k counterfactuals for each G_{t_i} s.t. $\Phi(G_{t_i}) = 1$
3:
4: – *Robust candidates identification* –
5: Get $\sigma_i = \sigma(G_{t_i})$ s.t. $\mathbf{1}[\sigma(G_{t_i}) \geq \theta] = \Phi(G_{t_i})\ \forall G_{t_i} \in \mathcal{G}$
6: **for** $G_{t_i} \in \mathcal{G}$ **do**
7: $\quad v_i \leftarrow \dfrac{\sum_{j=0}^{w-1} \left|\sigma_{\min(i+j+1,T)} - \sigma_{\min(i+j,T)}\right|}{t_{\min(i+w,T)} - t_i}$, as in Equation (4)
8: $\quad \delta_i \leftarrow \sqrt{{\sigma_i}^2 + {v_i}^2}$
9: **end for**
10: Compute $\mathcal{G}'$ as in Equation (5)
11: Compute $\mathcal{G}'_q$ as in Equation (6)
12:
13: – *Optimization to compute M_γ only once $\forall G_{t_j} \in \mathcal{G}'_q$* –
14: $\mathcal{T} \leftarrow [\,]$ *Initialize empty list*
15: **for** $G_{t_j} \in \mathcal{G}'_q$ **do**
16: $\quad$ Compute τ_j as in Equation (9)
17: $\quad \mathcal{T}[j] \leftarrow \tau_j$
18: **end for**
19: $\min_\tau \leftarrow \min(\mathcal{T})$, $\max_\tau \leftarrow \max(\mathcal{T})$
20: $\gamma \leftarrow \dfrac{\max_\tau - \mathcal{T}}{\max_\tau - \min_\tau}$ *Now γ is an array that has all taus normalized as in Equation* (10)
21:
22: – *Multi-objective selection* –
23: $cf \leftarrow \text{dict}()$ *Empty dictionary that is going to contain the top-k counterfactuals for each G_{t_i}*
24: $\alpha, \beta \leftarrow [[+\infty * |\mathcal{G}|] * |\mathcal{G}'_q|]$ *Initialize a matrix of dimensionality $|\mathcal{G}| \times |\mathcal{G}'_q|$ with elements equal to $+\infty$*
25: **for** $G_{t_i} \in \mathcal{G}$ s.t. $\Phi(G_{t_i}) = 1$ **do**
26: $\quad M \leftarrow +\infty * [|\mathcal{G}'_q|]$ *List of length $|\{\mathcal{G}'_q\}_{<t_i}|$ with all elements equal to $+\infty$*
27: $\quad$ **for** $G_{t_j} \in \{\mathcal{G}'_q\}_{<t_i}$ **do**
28: $\quad\quad \alpha[i,j] \leftarrow M_\alpha(G_{t_i}, G_{t_j})$
29: $\quad\quad \beta[i,j] \leftarrow M_\beta(G_{t_i}, G_{t_j})$
30: $\quad$ **end for**
31: $\quad$ Normalize $\alpha[i,:]$ and $\beta[i,:]$
32: $\quad M \leftarrow \alpha[i,:] + \beta[i,:] + \gamma$
33: $\quad \text{sort}(M, \text{ascending})$
34: $\quad cf[G_{t_i}] \leftarrow M[:k]$ *Take the first k elements, and return a list thereof*
35: **end for**
36: **return** cf

We assume that all initializations are done in constant time and do not contribute to the overall time complexity.

The identification of robust candidates (lines 5-11) is performed as a preprocessing step after the oracle has been trained. This step is executed only once, regardless of the number of anomalous instances to be explained. Let $P = |\mathcal{G}|$, $R = |\mathcal{G}'|$, $Q = |\mathcal{G}'_q|$, and the time complexity of querying Φ for the outcome of graphs equal to $\mathcal{O}(1)$ (i.e., line 5 costs $\mathcal{O}(1)$). We also consider the worst-case scenario in which $|\{\mathcal{G}'\}_{<t_i}| = |\mathcal{G}'| = R$, $|\{\mathcal{G}'_q\}_{<t_i}| = |\mathcal{G}'_q| = Q$.

The identification of robust candidates costs $\mathcal{O}(wP) = \mathcal{O}(P)$ since w is a constant. The computation of $\mathcal{G}'$ is $\mathcal{O}(1)$ since we already have calculated v_i and δ_i for each G_{t_i} in lines 6-9. The computation of $\mathcal{G}'_q$ costs $\mathcal{O}(R \log R)$ since the $\text{rank}^{\uparrow}_{\delta}$ function in Equation (6) can be seen as a sorting algorithm over $\mathcal{G}'$ in ascending order and then selecting the first q elements.

Before optimizing the multi-objective of Equation (11), we notice that, regardless of the input graph to be explained, the graphs in $\mathcal{G}'_q$ can have their M_γ computed a priori and only once (lines 14-20). To compute τ_j we can scan left-to-right and detect maximal contiguous runs of indices where $G_t \in \mathcal{G}'_q$. For a run of length h that starts at index s (i.e., indices $s, s+1, \dots s+h-1$ are in the set and $s+h$ is not or sequence ends), the permanence times are: $\tau_s = h-1, \tau_{s+1} = h-2, \dots, \tau_{s+h-1} = 0$. Filling these values costs $\mathcal{O}(h)$ for a run. Summed over runs this is $\mathcal{O}(Q)$ assuming that the membership $G_t \notin \mathcal{G}'_q$ is negligible. Hence, line 16 costs $\mathcal{O}(Q)$. Finding $\tau_{\min}$ and $\tau_{\max}$ costs $O(Q)$, and computing γ (line 20) costs $O(Q)$ since one can imagine this line to be an iteration over $\mathcal{G}'_q$ again to compute the gammas. Therefore, lines 14-20 cost $\mathcal{O}(Q+Q+Q) = \mathcal{O}(Q)$.

Let us now see how much computing M_α and M_β costs. Assuming that our graphs are memorized sparsely, computing their Laplacians costs $\mathcal{O}(e)$ where e is the number of edges. Then, the matrix multiplication between the Laplacian and the node feature vectors costs (naively) $\mathcal{O}(n^3)$ where n is the number of nodes. Hence the cost of M_α (line 28) is $\mathcal{O}(n^3+e) = \mathcal{O}(n^3)$. M_β (line 29) is just a simple difference between the time indices of two graphs and that can be done in $\mathcal{O}(1)$. Now, lines 27-30 cost $\mathcal{O}(n^3 Q)$. Line 31 costs $\mathcal{O}(Q)$ since it is just a simple min-max normalization and can be done similarly to lines 19-20. Line 32 is negligible. Line 33 costs $\mathcal{O}(Q \log Q)$ since the list M contains Q elements. Hence, the entire multi-objective selection procedure has a time complexity of $\mathcal{O}(P \cdot (n^3 Q + Q + Q \log Q)) = \mathcal{O}(n^3 PQ + PQ + PQ \log Q) = \mathcal{O}(n^3 PQ + PQ \log Q)$.

The total time complexity of CORTEX is $\mathcal{O}(P + R \log R + Q + n^3 PQ + PQ \log Q)$.

Since $Q < R < P$ and (assuming $Q \geq 2$) we have $\log Q \geq 1$:

- The lone P is dominated by $PQ \log Q$.
- The term Q is dominated by $PQ \log Q$ since $P > Q$.

Thus:

$$\mathcal{O}\big(P + R \log R + Q + n^3 PQ + PQ \log Q\big) = \mathcal{O}\big(PQ \log Q + n^3 PQ + R \log R\big)\,.$$

Factor PQ from the first two terms:

$$\mathcal{O}\big(PQ \log Q + n^3 PQ + R \log R\big) = \mathcal{O}\big(PQ\,(n^3 + \log Q) + R \log R\big)\,.$$

If $n^3 \gg \log Q$, then

$$\mathcal{O}\big(PQ\,(n^3 + \log Q) + R \log R\big) = \mathcal{O}\big(n^3 PQ + R \log R\big)\,.$$

Otherwise, the safe compact form is

$$\mathcal{O}\big(PQ\,(n^3 + \log Q) + R \log R\big)\,.$$

The proposed pipeline is built upon the GRETEL framework (Prado-Romero & Stilo, 2022). The source code for CORTEX is available at `https://anonymous.4open.science/r/CORTEX/`.

B Detailed Experimental Setup

CORTEX and SoTA were evaluated on a standard laptop (i.e., Intel Core i7-13th Gen, 10-Core 16-Thread 16GB RAM) as experiments do not require high-performance hardware.

Spatio-temporal graph construction. At each time step t_i, we define a graph G_{t_i} where each node u represents an EEG channel. We assign to each node a feature vector containing its normalized value at time t_i, along with values from the previous $m = 10$ time steps, each lagged by $\ell = 10$. We compute edge weights as the absolute value of the cross-correlation between each pair of EEG channels over a sliding window of the past $s = 5$ seconds. To prevent fully-connected graphs, we retain only the top $k_n = 4$ edges per node and symmetrize the adjacency matrix. We select these hyperparameters through patient-specific grid searches and choose the final configuration to maximize oracle accuracy across patients. We encode cross-correlations as edge weights, following prior work on GNNs for EEG data (Tian & Zhang, 2025; Abadal et al., 2025) and to capture temporal variations in inter-channel dependencies. We assign a binary label to each graph based on whether its time window includes any seizure activity. To address class imbalance, we apply non-uniform subsampling: we increase the sampling frequency during seizure periods and adjust it based on seizure duration. We exclude a total of 5% of each seizure window – equally split between the beginning and the end – to avoid unstable transitions that might blur class boundaries. This exclusion improves oracle accuracy while minimizing the amount of discarded data.

Oracle training. The design of the oracle does not have a direct influence on the overall pipeline. Its impact on the generated explanations is limited to its final outputs. Therefore, it is only important to ensure its accuracy. Here, we use a simple 2-layer Graph Convolutional Network (GCN) (Kipf & Welling, 2017), where node features of size d' are expanded to $4d'$ through the convolutional layers, and then mapped to the output via a fully-connected layer. A deeper investigation of the architecture would fall outside the scope of this work. Despite being trained on individual temporal snapshots, it is still possible to use our temporal approach for the explainer. To better capture individual variability and improve prediction accuracy, a separate oracle was independently trained for each patient using all EEG recordings for that subject. The performance metrics across recordings for each patient are reported in Section C.

Robust candidates identification. Once the oracle has been trained, we analyze the phase trajectory (σ, v) of its sigmoid outputs. This requires setting the parameter w, which defines the length of the temporal window used in Equation (4), and the parameter q, which determines the fraction of instances considered robust when defining the set $\mathcal{G}'_q$. These values must be calibrated based on the specific application. To guide this selection, we recommend examining the phase trajectory and the corresponding set of robust candidates $\mathcal{G}'_q$ graphically, as illustrated in Figures 4 and 5. In general, higher values of q result in a larger number of points in $\mathcal{G}'_q$, including points that may be less robust, which can cause the explainer to produce more variable results. In our experiments, we observed that varying w generally yields similar sets $\mathcal{G}'_q$. The main difference lies in the selection of points near the peaks of the sigmoid series: as w increases, the points in $\mathcal{G}'_q$ tend to be located progressively further from the peaks. Therefore, the choice of w should be guided by the level of robustness required for the specific case study. In our experiments, we set $w = 10$. The set of robust candidates $\mathcal{G}'_q$ is determined for each patient's EEG recording by selecting the $q = 25\%$ of points closest to $(0, 0)$ in terms of Euclidean distance.

Multi-objective selection criterion. Given an anomalous instance G_i from a specific EEG recording, we select the top $k = 5$ counterfactuals by minimizing the objective in Equation (11), which combines dissimilarity, temporal distance, and counterfactual robustness. A visual representation of the top-5 counterfactuals is provided in Section E.

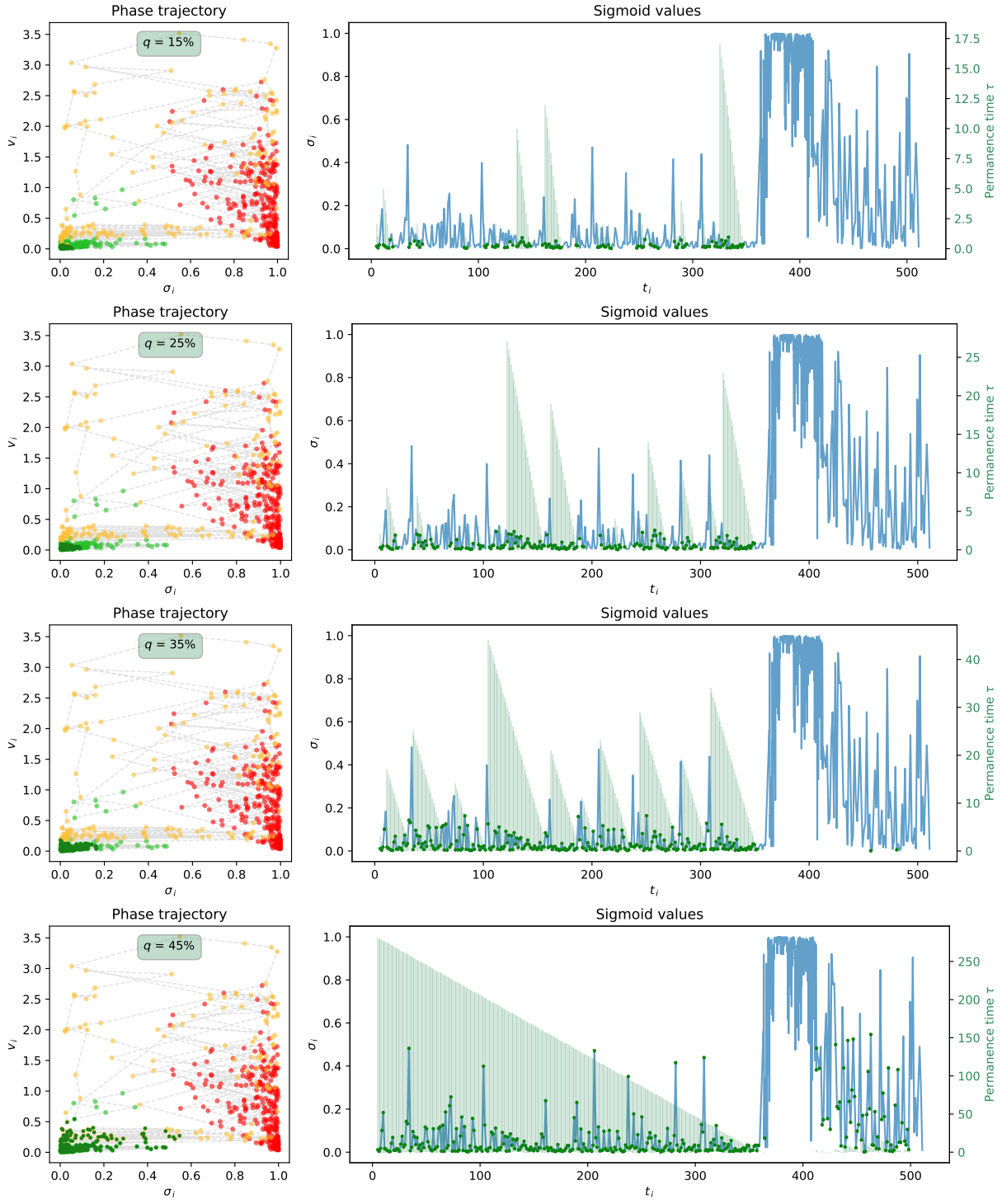

Figure 4: Sigmoid phase trajectory and points in $\mathcal{G}'_q$, as in Figure 3, for different values of q.

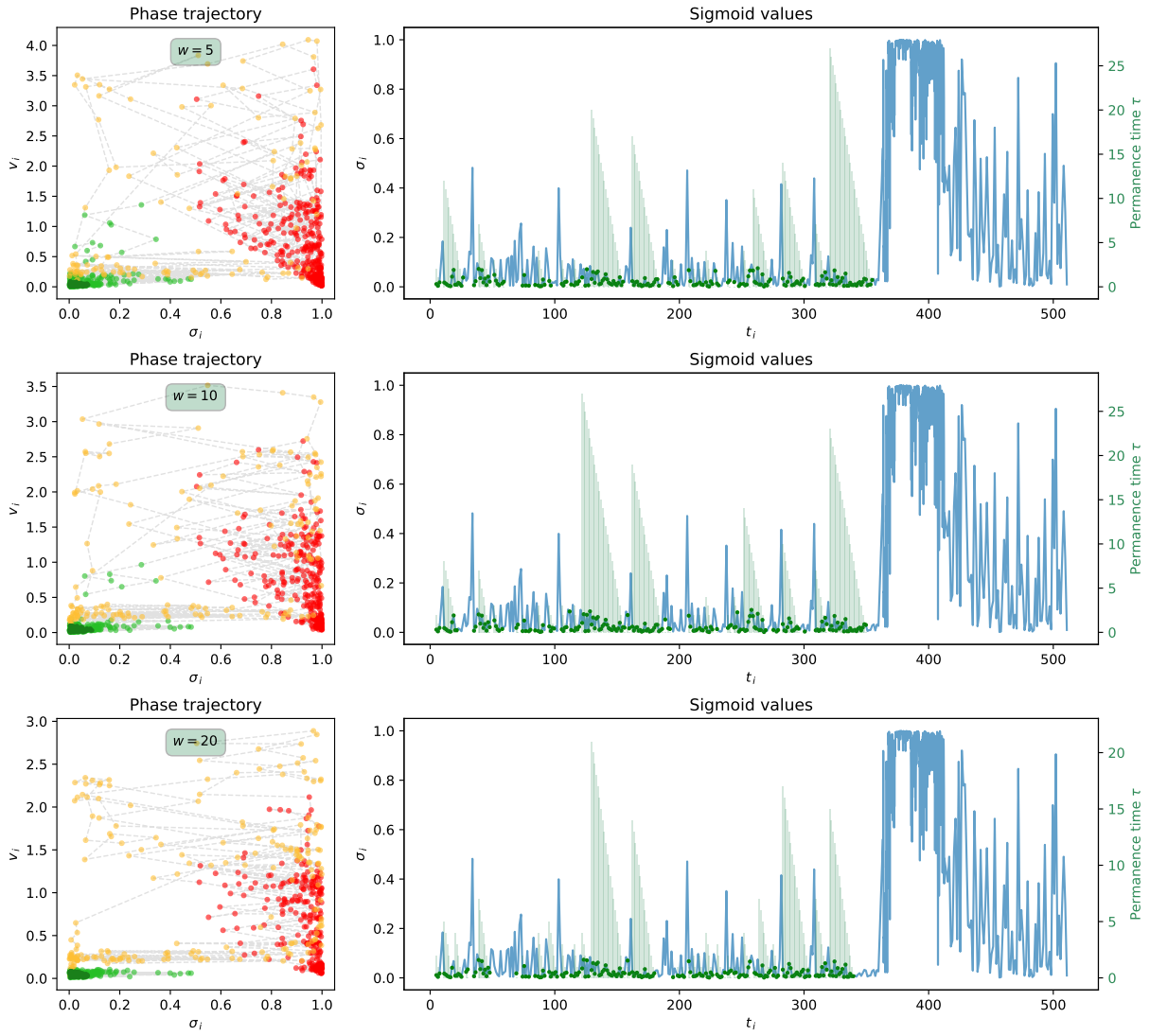

Figure 5: Sigmoid phase trajectory and points in $\mathcal{G}'_q$, as in Figure 3, for different values of w.

C Oracle Evaluation

Figure 6 shows accuracy, F1 score, precision, and recall of the oracles for each patient across individual EEG recordings.

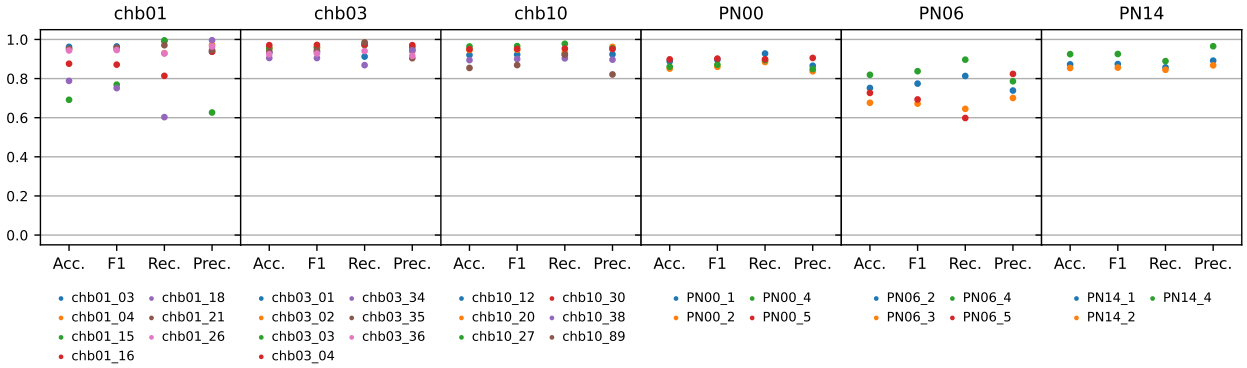

Figure 6: Evaluation metrics of the oracles for each patient (panels) across individual EEG recordings (points).

D Explainer Evaluation

The quality of counterfactual explanations can be assessed using different metrics, each capturing a different aspect of the explainer's performance (Prado-Romero et al., 2024b; Guidotti, 2022). Our evaluation criteria include validity, fidelity, dissimilarity, and implausibility, each calculated for every anomalous instance $G \in \mathcal{G}$ and its corresponding counterfactual G^*, then averaged over the entire dataset.

Validity indicates if the explainer has produced a valid counterfactual, and is defined as

$$\text{Validity}(G, G^*) = \mathbf{1}[\Phi(G) \neq \Phi(G^*)] \,, \tag{12}$$

where $\mathbf{1}[\cdot]$ denotes the indicator function.

Fidelity measures how much the explanations are faithful to the oracle, considering its validity. It is defined as

$$\text{Fidelity}_{\text{acc}}(G, G^*) = \mathbf{1}[\Phi(G) = y] - \mathbf{1}[\Phi(G^*) = y] \,, \tag{13}$$

where y is the true label associated to G (Yuan et al., 2023). A value of 1 indicates that both the explainer and the oracle are correct, while a value of 0 or -1 indicates an issue with either the explainer or the oracle. By focusing on the predicted probabilities, a more sensitive measure of fidelity can be computed as

$$\text{Fidelity}_{\text{prob}}(G, G^*) = \sigma(G)_y - \sigma(G^*)_y \,. \tag{14}$$

High values indicate better performance, as they reflect a substantial change in the prediction between G and G^*. Low values, instead, indicate little or no change, which may suggest that the generated counterfactual is invalid or adversarial. Unless otherwise specified, when we refer to *fidelity*, we mean $\text{Fidelity}_{\text{prob}}$ as defined in Equation (14).

Dissimilarity quantifies the closeness between an instance and its counterfactual. Here, M_α serves as the dissimilarity measure, as defined in Equation (7).

Implausibility is given by the minimum distance of the counterfactual G^* from the closest example in a reference population $\mathcal{R}$:

$$\text{Implausibility}(G^*) = \min_{G \in \mathcal{R}} D(G^*, G) \,. \tag{15}$$

Here, the distance $D(\cdot, \cdot)$ is again represented by the dissimilarity measure M_α. In our setting, when evaluating the implausibility of a counterfactual $G^*_{t_i}$ for an anomalous instance G_{t_i}, the reference population $\mathcal{R}$ is

chosen to comprise all graphs in the dataset $\mathcal{D}$ observed before t_i that were classified as 0 by the oracle. This ensures that the implausibility reflects how different the counterfactual is with respect to past instances of the target class. The use of the minimum distance, rather than an average, follows the formulation used by Guidotti (2022), where implausibility is interpreted as the deviation from the most similar instance in the reference population.

Ideal values for these metrics are validity and fidelity equal to 1, and implausibility and dissimilarity equal to 0. By design, CORTEX always generates valid and plausible counterfactuals. Therefore, validity and fidelity are only related to the oracle accuracy, while implausibility is always equal to zero. We include these metrics primarily for historical reasons and because they are considered standard in the literature.

In our results, we report validity and fidelity averaged only over correctly classified instances, and dissimilarity and implausibility averaged only over instances where $\text{Fidelity}_{\text{acc}} = 1$.

Table 4 reports the average implausibility and dissimilarity of the top-1 counterfactuals for each individual EEG recording, both computed only for explanations with $\text{Fidelity}_{\text{acc}}$ equal to 1, in order to avoid bias from incorrect counterfactuals. GNN-MOExp is excluded from the table, as its dissimilarity and implausibility are undefined.

Table 4: Average implausibility and dissimilarity of top-1 counterfactuals for individual EEGs. Lowest values in bold.

`chb01_03` (oracle accuracy: 0.9621)		
Explainer	Implausibility	Dissimilarity
OBS	1.2003	0.4365
DDBS	0.9309	**0.2715**
CORTEX	**0**	1.7816

`chb01_04` (oracle accuracy: 0.9501)		
Explainer	Implausibility	Dissimilarity
OBS	1.2775	0.3717
DDBS	1.1972	**0.2787**
CORTEX	**0**	1.4246

`chb01_15` (oracle accuracy: 0.6915)		
Explainer	Implausibility	Dissimilarity
OBS	1.4889	0.4725
DDBS	1.2815	**0.3156**
CORTEX	**0**	1.6931

`chb01_16` (oracle accuracy: 0.8760)		
Explainer	Implausibility	Dissimilarity
OBS	1.4973	0.4974
DDBS	1.4046	**0.4083**
CORTEX	**0**	1.6016

`chb01_18` (oracle accuracy: 0.7883)		
Explainer	Implausibility	Dissimilarity
OBS	0.8399	0.1922
DDBS	0.8054	**0.1605**
CORTEX	**0**	0.9082

`chb01_21` (oracle accuracy: 0.9518)		
Explainer	Implausibility	Dissimilarity
OBS	0.9665	0.5331
DDBS	0.8461	**0.4181**
CORTEX	**0**	1.1320

`chb01_26` (oracle accuracy: 0.9437)		
Explainer	Implausibility	Dissimilarity
OBS	1.1791	0.3326
DDBS	1.0719	**0.2404**
CORTEX	**0**	1.2709

`chb03_01` (oracle accuracy: 0.9336)		
Explainer	Implausibility	Dissimilarity
OBS	0.4121	0.1101
DDBS	0.3731	**0.0773**
CORTEX	**0**	0.4476

`chb03_02` (oracle accuracy: 0.9550)		
Explainer	Implausibility	Dissimilarity
OBS	0.6800	0.2233
DDBS	0.5273	**0.1025**
CORTEX	**0**	0.8432

`chb03_03` (oracle accuracy: 0.9554)		
Explainer	Implausibility	Dissimilarity
OBS	0.8045	0.2170
DDBS	0.7965	**0.1897**
CORTEX	**0**	0.9130

`chb03_04` (oracle accuracy: 0.9708)		
Explainer	Implausibility	Dissimilarity
OBS	0.0519	0.2992
DDBS	1.0217	**0.2422**
CORTEX	**0**	1.1333

`chb03_34` (oracle accuracy: 0.9052)		
Explainer	Implausibility	Dissimilarity
OBS	0.9624	0.2567
DDBS	0.7707	**0.1644**
CORTEX	**0**	1.2208

`chb03_35` (oracle accuracy: 0.9376)		
Explainer	Implausibility	Dissimilarity
OBS	0.8425	0.2537
DDBS	0.6000	**0.1428**
CORTEX	**0**	1.1962

`chb03_36` (oracle accuracy: 0.9246)		
Explainer	Implausibility	Dissimilarity
OBS	0.8376	0.2489
DDBS	0.7162	**0.1630**
CORTEX	**0**	1.2513

`chb10_12` (oracle accuracy: 0.9206)		
Explainer	Implausibility	Dissimilarity
OBS	0.5573	0.1416
DDBS	0.5312	**0.1027**
CORTEX	**0**	0.6643

`chb10_20` (oracle accuracy: 0.9462)		
Explainer	Implausibility	Dissimilarity
OBS	0.5905	0.1370
DDBS	0.4842	**0.0808**
CORTEX	**0**	0.8033

`chb10_27` (oracle accuracy: 0.9641)		
Explainer	Implausibility	Dissimilarity
OBS	0.7422	0.1894
DDBS	0.4877	**0.0813**
CORTEX	**0**	1.1736

`chb10_30` (oracle accuracy: 0.9501)		
Explainer	Implausibility	Dissimilarity
OBS	0.9513	0.2093
DDBS	0.8693	**0.1410**
CORTEX	**0**	1.1082

chb10_38 (oracle accuracy: 0.8943)		
Explainer	Implausibility	Dissimilarity
OBS	1.0010	0.2314
DDBS	0.8795	**0.1394**
CORTEX	**0**	1.4398

chb10_89 (oracle accuracy: 0.8544)		
Explainer	Implausibility	Dissimilarity
OBS	0.9088	0.2243
DDBS	0.8168	**0.1633**
CORTEX	**0**	1.1030

PN00_1 (oracle accuracy: 0.8876)		
Explainer	Implausibility	Dissimilarity
OBS	1.3047	1.0654
DDBS	1.2586	**1.0256**
CORTEX	**0**	1.3237

PN00_2 (oracle accuracy: 0.8508)		
Explainer	Implausibility	Dissimilarity
OBS	0.9925	0.9394
DDBS	0.8648	**0.7789**
CORTEX	**0**	0.8519

PN00_4 (oracle accuracy: 0.8608)		
Explainer	Implausibility	Dissimilarity
OBS	1.0833	0.9085
DDBS	1.0034	**0.8186**
CORTEX	**0**	1.1169

PN00_5 (oracle accuracy: 0.8983)		
Explainer	Implausibility	Dissimilarity
OBS	0.3960	0.2386
DDBS	0.3816	**0.2168**
CORTEX	**0**	0.4756

PN06_2 (oracle accuracy: 0.7519)		
Explainer	Implausibility	Dissimilarity
OBS	0.0946	0.0453
DDBS	0.0910	**0.0411**
CORTEX	**0**	0.1386

PN06_3 (oracle accuracy: 0.6764)		
Explainer	Implausibility	Dissimilarity
OBS	0.0673	0.0438
DDBS	0.0634	**0.0367**
CORTEX	**0**	0.2333

PN06_4 (oracle accuracy: 0.8192)		
Explainer	Implausibility	Dissimilarity
OBS	0.1979	0.0915
DDBS	0.1917	**0.0820**
CORTEX	**0**	0.2736

PN06_5 (oracle accuracy: 0.7268)		
Explainer	Implausibility	Dissimilarity
OBS	0.1925	0.0972
DDBS	0.1816	**0.0924**
CORTEX	**0**	0.4209

PN14_1 (oracle accuracy: 0.8727)		
Explainer	Implausibility	Dissimilarity
OBS	0.1463	0.0470
DDBS	0.1385	**0.0404**
CORTEX	**0**	0.2330

PN14_2 (oracle accuracy: 0.8538)		
Explainer	Implausibility	Dissimilarity
OBS	0.1368	0.1020
DDBS	0.1350	**0.0971**
CORTEX	**0**	0.1970

PN14_4 (oracle accuracy: 0.9248)		
Explainer	Implausibility	Dissimilarity
OBS	0.6103	**0.2448**
DDBS	0.6850	0.2837
CORTEX	**0**	1.0545

OBS and DDBS consistently show lower dissimilarity scores, but these are often associated with higher implausibility, indicating that the generated counterfactuals are structurally less realistic. CORTEX, instead, achieves zero implausibility by design, as it searches counterfactuals within the dataset. We stress that implausibility is the primary factor in the evaluation: when implausibility is high, dissimilarity becomes uninformative, as proximity to the original graph cannot compensate for a lack of plausibility.

E Visualization of Explanations

Here we provide graphical representations that offer both a global and a detailed view of the topological changes in the counterfactual explanations compared to the original instance. All the visualizations refer to the same anomalous instance from record chb03_01.

Figure 7 provides a summarized view of the top-5 counterfactuals for an anomalous instance by highlighting edges that are consistently added or removed across all of them. This summary helps identify structural changes that appear in most (or all) counterfactuals, which may correspond to meaningful topological changes rather than random variations. Figure 8 details the topology of each of the top-5 counterfactuals, highlighting added, removed, and preserved edges. Finally, Figure 9 offers a more detailed comparison of edge weights between the original graph and its counterfactuals.

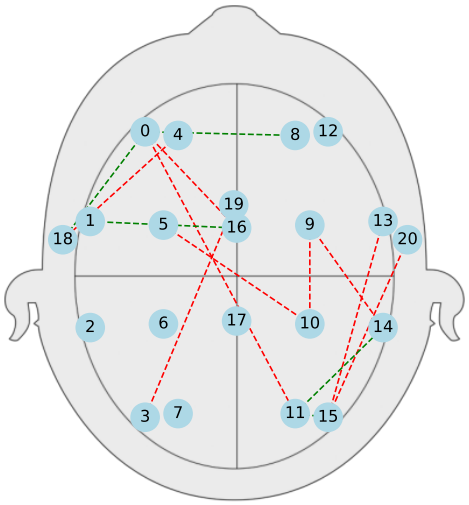

Figure 7: Visualization of edges consistently added (green) or removed (red) across the top-5 counterfactuals for an anomalous instance. Example from record `chb03_01`.

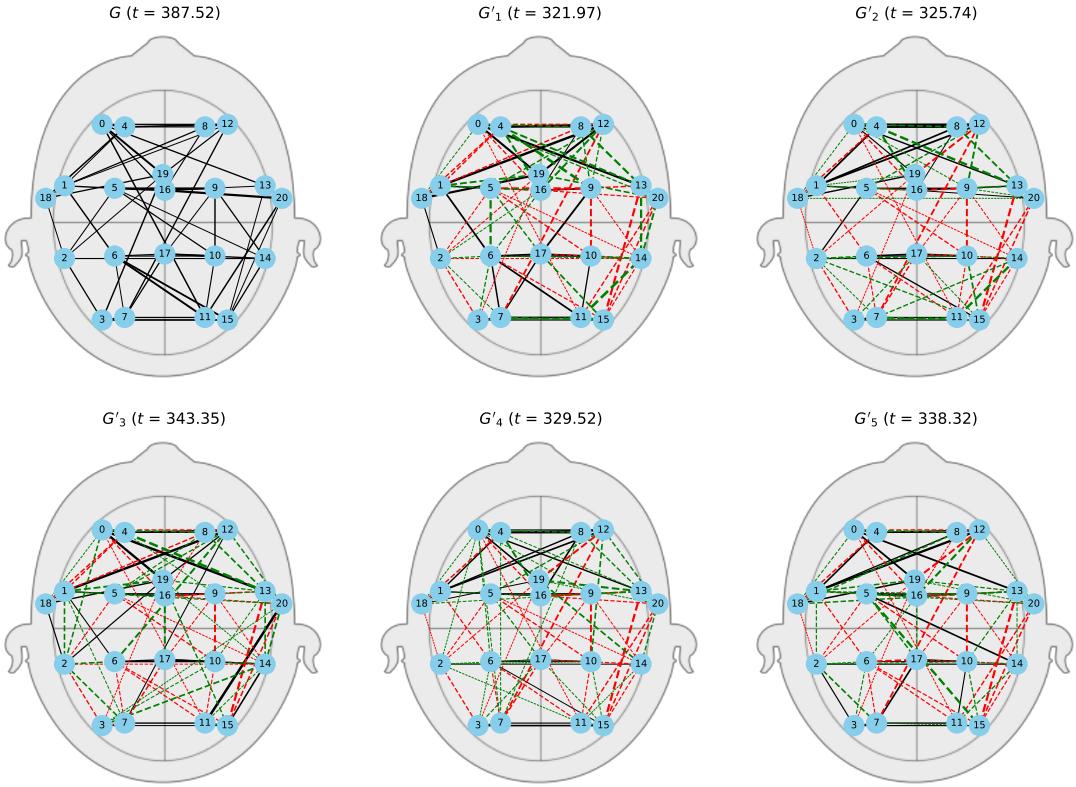

Figure 8: Comparison between an anomalous instance and its top-5 counterfactuals. Black edges are preserved, red dashed edges are removed from the original graph, and green dashed edges are added in the counterfactuals. Edge thickness is proportional to the corresponding weight. Example from record `chb03_01`.

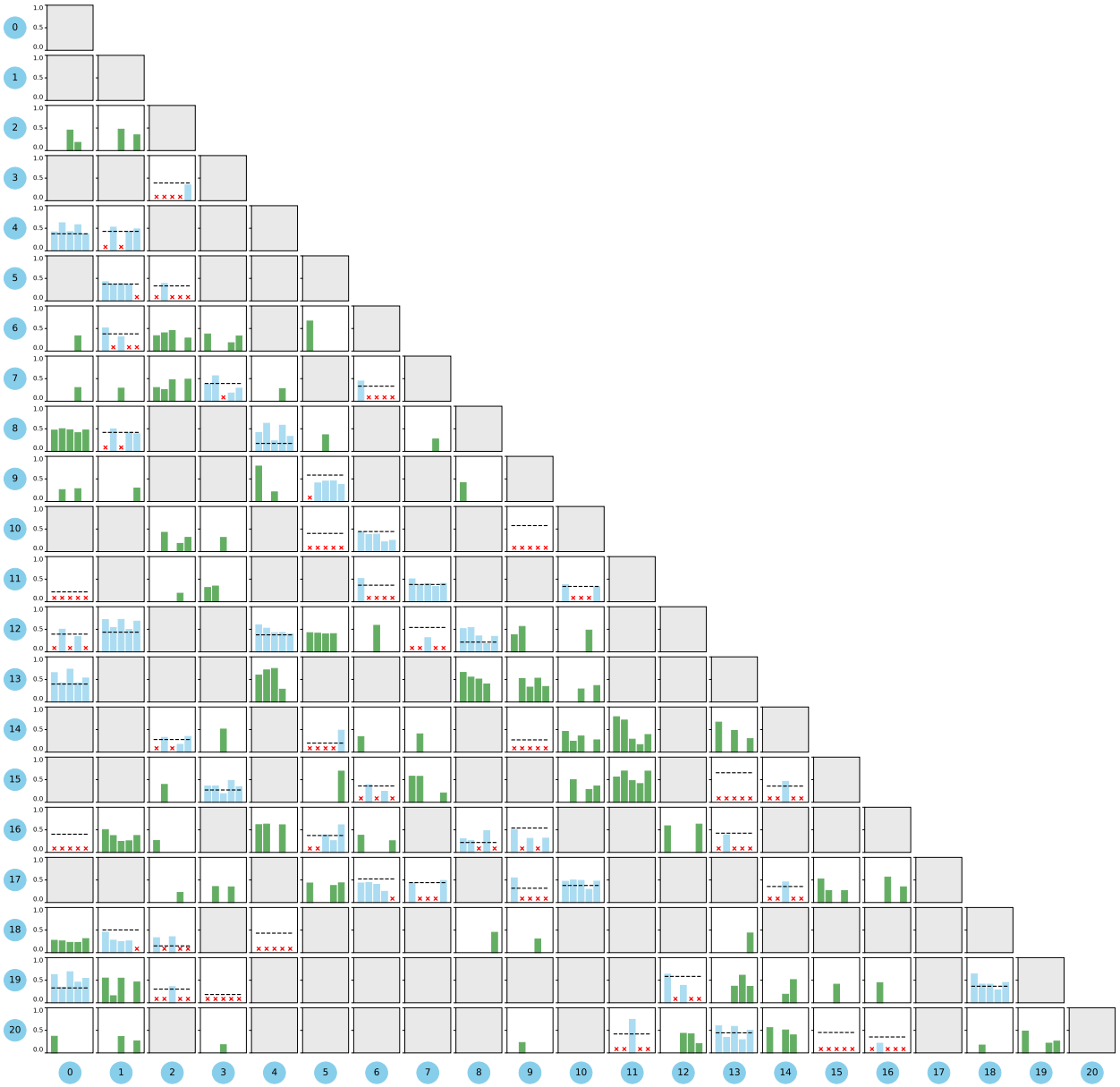

Figure 9: Edge weights of an anomalous instance and its top-5 counterfactuals. Each cell corresponds to an undirected edge between two nodes, with node labels shown along the axes. The dashed line shows the original weight, while vertical bars indicate the corresponding edge weights in the counterfactuals (green bars for added edges, red crosses for removed edges, and blue bars for modified edges). Example from record `chb03_01`.